Optics Communications 285 (2012) 4632–4637

Contents lists available at SciVerse ScienceDirect

Optics Communications

journal homepage: www.elsevier.com/locate/optcom

Morphological characterization of cells in concentrated suspensions using multispectral diffuse optical tomography

Mohammad Reza Hajihashemi, Xiaoqi Li, Huabei Jiang*

Department of Biomedical Engineering, University of Florida, Gainesville, FL, USA

ARTICLE INFO

Article history:
Received 26 October 2011
Received in revised form
9 July 2012
Accepted 10 July 2012
Available online 26 July 2012

Keywords:
Cellular imaging
Diffuse optical tomography
T-matrix method
Red blood cells

ABSTRACT

Based on a non-spherical model of particle scattering, we investigate the capabilities and limitations of a T-matrix based inverse algorithm to morphologically characterize cells in concentrated suspensions. Here the cells are modeled as randomly orientated spheroidal particles with homogenous dielectric properties and suspended in turbid media. The inverse algorithm retrieves the geometrical parameters and the concentration of cells simultaneously by inverting the reduced scattering coefficient spectra obtained from multispectral diffuse optical tomography (MS-DOT). Both round and spheroidal cells are tested and the role of multiple and higher order scattering of particles on the performance of the algorithm is evaluated using different concentrations of cells.

1. Introduction

Morphological characterization of cells plays an important role in clinical diagnosis [1–6]. For example, tumorous cells are crowded and enlarged compared to normal cells [1]. Microscopy is routinely used to examine the cellular morphology, but it is not applicable to *in vivo* tissue. It has been shown that multispectral diffuse optical tomography (MS-DOT) is a promising modality for imaging of cellular morphology since it is non-invasive and can be used to characterize *in vivo* cells located deep in tissue [7]. The basic idea of MS-DOT is to illuminate the tissue by near-infrared light and collect the scattered light along the tissue boundary. By analyzing the spectra of scattered light, one can retrieve information regarding the morphology and composition of cells.

It is known that MS-DOT or other optical based particle sizing methods are dealing with an ill-posed inverse problem that requires some *a priori* information about the cells in order to obtain stable and unique solutions [7,8]. For example, the spherical model of the Mie scattering theory is widely used so far. However, cells generally have complex irregular shapes; thus the effect of non-sphericity cannot be adequately addressed by the Mie based techniques [9]. This necessitates a non-spherical model of particle scattering for accurate cellular sizing. The T-matrix or extended boundary conditions method is one of the most powerful and widely used tools for rigorous computation of electromagnetic scattering by single or an aggregate of non-spherical particles [10,11]. In the T-matrix approach, the incident and scattered waves are expanded in terms of incoming and outgoing vector spherical wave functions. The relationship between the coefficient of the incident and scattered waves is established through a transmission matrix (i.e., the T-matrix). The main advantage of T-matrix representation is that it is independent of the incident/scattered wave directions and that it depends only on the shape, size, orientation and refractive index of the particles [10].

The application of the T-matrix method to assess the morphology of spheroidal particles has been reported in several publications [12–14]. However, these studies did not demonstrate the ability to retrieve the concentration of particles or the methods used were not applicable for characterization of cell aggregates in deep tissue. The purpose of our current work is to demonstrate and evaluate our MS-DOT-T-matrix based inverse algorithm for characterization of cells in concentrated suspensions. In our method, the scattering spectra of cell suspensions provided by MS-DOT are used to retrieve the statistical parameters of cells including mean size, volume fraction and aspect ratio through the T-matrix based algorithm. Both round and spheroidal cells embedded in turbid media are studied. This work is the first demonstrating the application of MS-DOT for morphological characterization of cells suspended in a culture medium, by analyzing diffusely scattered light collected along the phantom boundary.

2. Methodology

2.1. Theoretical summary and the inverse algorithm

The first step in our technique is to shine laser beams into a mixture containing the cells to be characterized. The light sources

* Corresponding author.
E-mail address: hjiang@bme.ufl.edu (H. Jiang).

0030-4018/$ - see front matter © 2012 Elsevier B.V. All rights reserved.
http://dx.doi.org/10.1016/j.optcom.2012.07.043

are placed sufficiently far from the suspensions. The presence of cells influences light scattering and propagation within the suspensions. Afterwards, photon densities along the medium boundary are recorded by some detectors for further analysis. We suppose that cells have spheroidal shapes and they are dispersed in suspensions with random orientations.

The photon propagation in suspensions satisfies the following photon diffusion equation, which can be rigorously solved by the finite element method [7]:

$$\nabla\cdot(D(r)\Phi(r,\omega))-[\mu_a(r)-i\omega/c]\Phi(r,\omega)=-S(r,\omega) \quad (1)$$

where $\Phi(r,\omega)$ is the photon density, ω is the angular frequency, $D(r)=1/3(\mu_a(r)+\mu_s'(r))$ is the diffusion coefficient, $\mu_a(r)$ is the absorption coefficient, $\mu_s'(r)$ is the reduced scattering coefficient, c is the speed of light in the medium, $S(r,\omega)$ is the source term, and an $\exp(-i\omega t)$ time variation is assumed. Once the reduced scattering spectra are recovered using the MS-DOT algorithm, as elaborated in Ref. [7], they have to be further processed to recover the morphological parameters of the cells.

At each computational node, the measured reduced scattering coefficient is related to the particle morphology parameters through the following expression:

$$\mu_s'(\lambda)=\phi\int_{r=r_{\min}}^{r=r_{\max}}\int_{\varepsilon=\varepsilon_{\min}}^{\varepsilon=\varepsilon_{\max}}\frac{e^{-(1/2)\left(\frac{(r-r_m)^2}{\delta_m^2}+\frac{(\varepsilon-\varepsilon_m)^2}{\delta_\varepsilon^2}\right)}}{2\pi\delta_r\delta_\varepsilon}\left(1-\frac{\alpha_1^1(r,\varepsilon)}{3}\right)\langle C_{sca}(r,\varepsilon)\rangle\,dr\,d\varepsilon \quad (2)$$

The reduced scattering coefficient, at a wavelength λ, is denoted by the symbol $\mu_s'(\lambda)$. $r\in[r_{\min}r_{\max}]$ is the equal-volume radius of the scattering particle. $\varepsilon\in[\varepsilon_{\min}\varepsilon_{\max}]$ is the aspect ratio, which is the fraction of the equatorial radius to the polar radius of the spheroidal particle. We have utilized a bivariate normal distribution function to describe the random variations in the cell size and aspect ratio. The mean values of the particle radius and aspect ratio are represented by the symbols r_m and ε_m, respectively. The concentration of cells is represented by the symbol ϕ , which represents the number of cells per cubic millimeter. The following relationship holds between the cell volume fraction and its concentration:

$$VF\,(\%)=0.1\phi\ (\text{in million per cubic millimeter})\times\frac{4\pi}{3}r_m(\text{in }\mu m^3) \quad (3)$$

δ_r and δ_ε are the standard deviations of the cell size and aspect ratio, respectively. In this work we assumed that the standard deviations are 10% of their corresponding mean values. $\langle C_{sca}(r,\varepsilon)\rangle$ denotes the averaged scattering cross section which can be calculated using the T-matrix method. $\alpha_1^1(r,\varepsilon)$ is a coefficient obtained by expanding the phase function [15]. The values of $\langle C_{sca}(r,\varepsilon)\rangle$ and $\alpha_1^1(r,\varepsilon)$ are *a priori* calculated and stored in a T-matrix database.

In order to recover the cell size ($2r_m$), aspect ratio (ε_m) and the concentration (ϕ), we first need to find the best estimates for these parameters, in a range of their possible values, by minimizing the error function $\chi^2=\sum_{\lambda_j}(\mu_s'(\lambda_j)^o-\mu_s'(\lambda_j)^c)^2$, where $\mu_s'(\lambda_j)^o$ is the observed reduced scattering coefficient and $\mu_s'(\lambda_j)^c$ is the calculated one from Eq. (2) and $\lambda_j\ j=1,2\ \ldots$ are the measurement wavelengths.

The updates for unknown parameters are determined by solving

$$(J^TJ+\gamma I)\Delta\zeta=J^T\Delta\chi \quad (4)$$

where γ is an appropriately chosen regularization parameter, I is the identity matrix, the vector $\Delta\chi=[\mu_s'(\lambda_1)^o-\mu_s'(\lambda_1)^c,\ldots]^T$ represents the error between the observed and calculated reduced scattering coefficients and $\Delta\zeta=[\Delta\phi\quad\Delta\delta_r\quad\Delta r_m\quad\Delta\delta_\varepsilon\quad\Delta\varepsilon_m]^T$ is the vector which updates the parameters of interest. We can obtain explicit expressions for the elements of the Jacobian matrix J by direct differentiation of Eq. (2) with respect to the model parameters.

2.2. Experimental setup and data collection

Briefly, light from one of the five continue-wave laser modules was transmitted to an optical switch, which sequentially passes it to 16 pre-selected points at the surface of the phantom for 2D imaging experiments. 16×16 measured data was then input into our MS-DOT reconstruction algorithm to generate a 2D cross-sectional image of the phantom [7]. Measurement data at five wavelengths of 733, 775, 808, 840, and 915 nm were used for the image reconstructions.

For cellular sizing, depending on the cell type and its refractive index, an *a priori* stored T-matrix database with different combinations of cell size and aspect ratio was used to calculate the reduced scattering coefficient [16] and recover the unknown morphological parameters using the inverse algorithm [15]. A separate T-matrix database was used for characterization of the scattering Intralipid particles in the background [17,18]. Cells to be characterized were suspended in a glass tube which was embedded off-center in the cylindrical background phantom consisting of 1% Intralipid and India Ink (Fig. 1).

3. Results and discussion

3.1. Chinese Hamster Ovary (CHO) cells

CHO cells are one of the most commonly used cell cultures in biological and medical researches. CHO cells have epithelial morphology in culture and grow attached to the surface of a flask. While attached to the surface, CHO cells have polygonal and elongated shapes as shown in Fig. 2a. The size of CHO cells is about 14–15 μm with refractive index of ~1.38 [19–21]. Optical scattering from CHO cells cannot be accurately measured while they are attached to the plastic surface. Hence, we utilized a serum free medium to suspend CHO cells following the procedure described in Ref. [22]. While in suspension, the irregular-shaped CHO, being anchorage-dependent cells, change their morphology

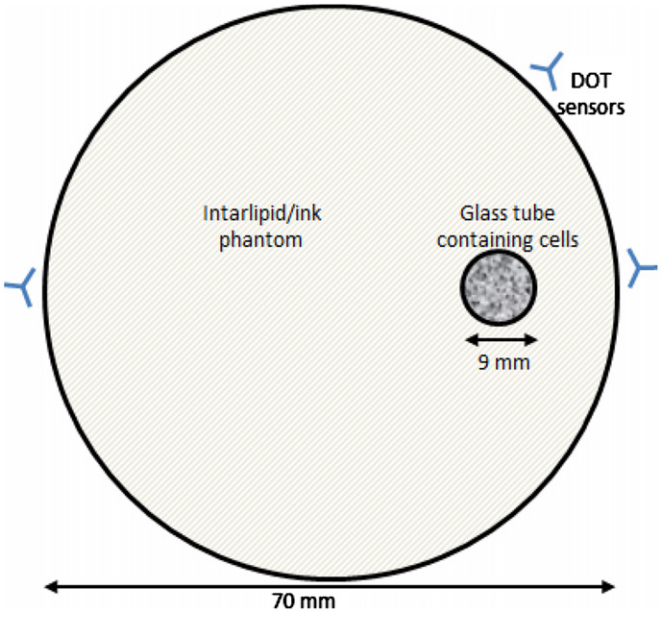

Fig. 1. Diagram of the experimental setup for MS-DOT measurements.

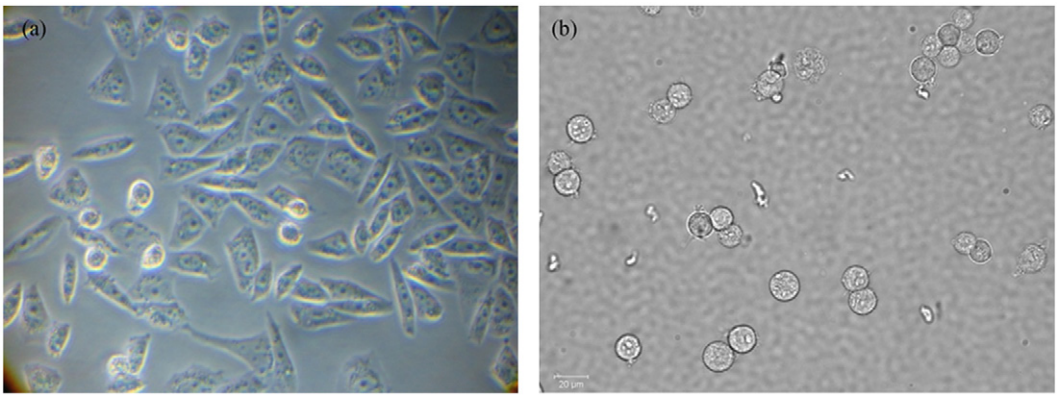

Fig. 2. (a) CHO cells attached to the plastic surface, and (b) CHO cells suspended in serum free medium.

Table 1
Averaged reduced scattering coefficients at five wavelengths of interest (mm^{-1}).

	733 (nm)	775 (nm)	808 (nm)	840 (nm)	915 (nm)
CHO cells/target	0.145	0.146	0.142	0.142	0.149
Background	0.202	0.204	0.205	0.205	0.209

and become rounded. As shown in Fig. 2b, CHO cells have almost spherical shapes in serum free medium.

The T-matrix database was generated for cells with size ranging from 3 to 9 μm in equivalent radius, and 0.8–1.2 in aspect ratio [16]. The background was a 70 mm diameter cylindrical solid phantom made of Intralipid and India ink, and had an absorption coefficient of 0.005 mm^{-1} and a reduced scattering coefficient of ~0.2 mm^{-1}. A 9 mm diameter glass tube, containing CHO cells, was embedded 20 mm away from the center of the background phantom. Table 1 gives the averaged reduced scattering coefficient of CHO cells/target and the background phantom at five wavelengths of interest. The presented data show that the background phantom had higher scattering coefficient compared with the target due to relatively low concentration of CHO cells used. Fig. 3a, c and e, respectively, show the recovered images of particle size, concentration and aspect ratio using our T-matrix based algorithm. For better quantitative assessment, each of the recovered parameters is also plotted along a line passing through the centers of the background and target (Fig. 3b, d, and f).

According to Fig. 3a and b, the recovered size of CHO cells is about 14 μm, in good agreement with that measured by microscopy (Fig. 2b). The aspect ratio images (Fig. 3e and f) demonstrate that the cells in the target and the Intralipid particles in the background are spherical in shape. Again, this agrees well with those measured by microscopy for both the cells (Fig. 2b) and Intralipid [17]. The concentration of CHO cells used in our experiments could not be accurately measured using microscopy, but we estimate from the reconstructed value of volume fraction (Fig. 3c and d) that the recovered concentration of CHO cells is ~60,000 cells/mm^3.

3.2. Red blood cells

Erythrocytes or human red blood cells (RBCs) as targets with different concentrations were also examined. Unlike mammalian cells such as CHO, RBCs retain their non-spherical shape in isotonic solutions (with the same salt concentration of blood cells). Normal saline solution (0.9% NaCl) is considered isotonic with blood cells. Therefore, RBCs are a good candidate to demonstrate the capability of our algorithm in retrieving the morphological parameters of non-spherical cells.

The optical properties of individual RBCs and compounded blood samples were studied previously [23–26]. The size of RBCs is in the range 6–7 μm with a relative refractive index of ~1.05 compared to the surrounding saline medium. In the optical study of RBCs, RBCs are typically represented by homogenous volume-equivalent oblate spheroids [25]. In our study the T-matrix database for RBCs was generated with particle size of 2–8 μm and aspect ratio of 0.4–4. Fig. 4 presents the microscopic images of RBCs suspended in saline solution with three different volume fractions of 9%, 16% and 33%. As shown in Fig. 4, when the concentration of RBCs increases, the average distance between cells decreases subsequently, and some cells are tightly attached to each other or significantly deformed (Fig. 4c) compared to the lower concentration cases (Fig. 4a and b).

MS-DOT experiments were conducted when RBC suspensions of different concentrations were embedded in the Intralipid/ink background phantom. Table 2 lists the averaged reduced scattering coefficients of the RBCs/target of three different concentrations/volume fractions at three wavelengths of interest.

It is worth noticing that when the concentration of RBCs is increased from 9% to 16%, the corresponding scattering coefficient increases almost proportionally. However, when the concentration of RBCs is increased from 16% to 33%, this linearity breaks down. Fig. 5 shows the retrieved images of particle size, concentration and aspect ratio for the three cases of RBCs. Here the particle size is defined as the diameter of sphere with an equal volume of oblate RBCs.

From the results shown in Fig. 5, the recovered equivalent size and aspect ratio of RBCs are ~4.5–5 μm and ~2.3, respectively, resulting in an equatorial diameter of 6–6.5 μm for the RBCs. This is quantitatively consistent with that measured by microscopy (see Fig. 4) and that available from literature [25]. The concentration images shown in Fig. 5b and e demonstrate that the recovered volume fractions of RBCs are almost the same as the actual values in saline solution (i.e., 9% and 16%). However, when the actual concentration of RBCs is increased to 33%, the retrieved volume fraction of the RBCs is only 18% (see Fig. 5h). This large error in volume fraction (15%) is mainly caused by interactions between the cells in highly concentrated suspensions that are not included in our current T-matrix based method [15].

In low to moderately concentrated suspensions, the distances among particles are relatively large and the interactions between neighboring particles can be ignored. In such cases, the reduced scattering coefficient is linearly proportional to the concentration of particles. As the concentration of particles within the suspensions is increased, the particle–particle interactions become significant and the reduced scattering coefficient is no longer a linear function of particle concentration. Compared with low to moderately concentrated suspensions, the scattering efficiency is substantially reduced for highly concentrated suspensions [27].

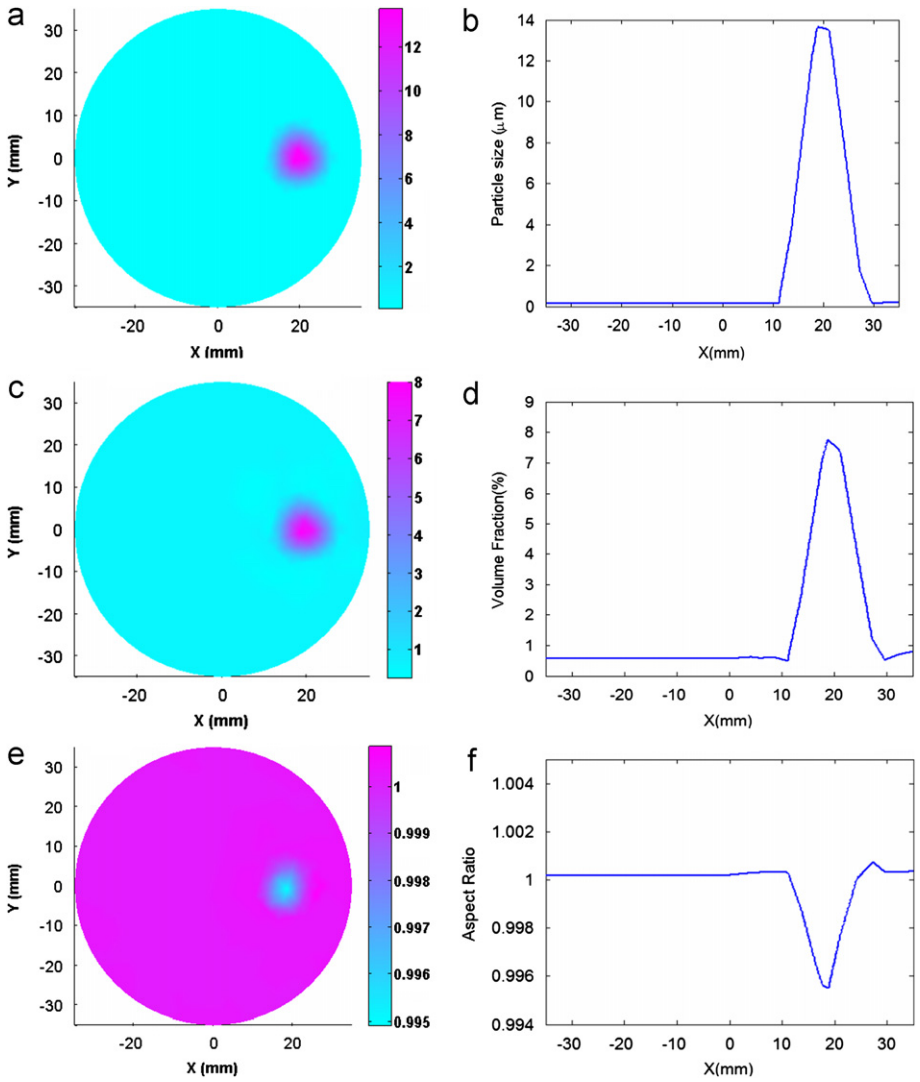

Fig. 3. Reconstructed particle size (a, b), concentration (c, d), and aspect ratio (e, f) of CHO cells.

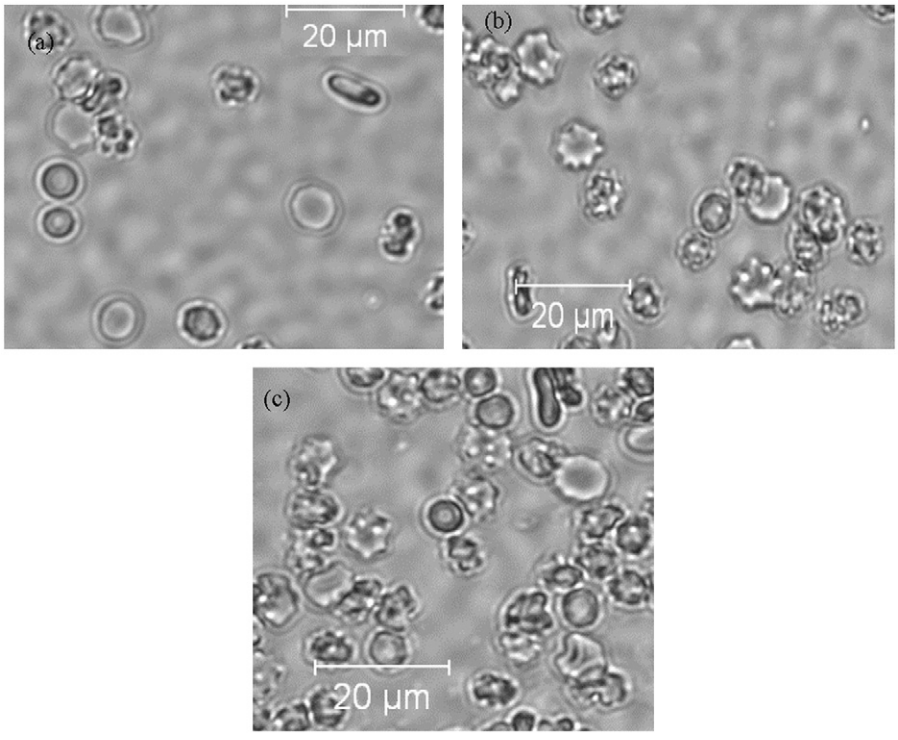

Fig. 4. RBCs in saline with (a) 9% VF, (b) 16% VF, and (c) 33% VF.

As shown in previous studies [27,28], when the volume fraction of particles reached ~10%, the corresponding scattering coefficient saturated and further increment of volume fraction did not increase the scattering coefficient. In order to account for this effect, static and angle-integrated structure factors were introduced and incorporated into their Mie-based scattering model. Consequently, improvements were obtained in calculation of the reduced scattering coefficient in highly concentrated suspensions of particles (up to 40% in volume fraction) [28].

The absorption coefficient is not directly used in this work since it is a measure of the percent of energy not scattered/reflected. However, the absorption should be small since a greater amount of photons are scattered and detected by the light detectors, rather than absorbed in the medium. Therefore, we only process the reduced scattering spectra in order to extract the morphological parameters of cells in suspensions.

Table 2
Averaged reduced scattering coefficients at three wavelengths of interest (mm^{-1}).

	808 (nm)	840 (nm)	915 (nm)
9% VF	0.6942	0.6280	0.6279
16% VF	1.7146	0.7163	1.0417
33% VF	1.7884	1.2616	1.1515

In all examples presented in this work, the absorption coefficient is much smaller than the reduced scattering coefficient. Compared with CHO cells, red blood cells (RBC) absorb the diffused light more strongly. However, the absorption coefficients for RBCs are still several orders of magnitude smaller than the scattering coefficients in the near infrared range [26].

Our algorithm has relatively robust performance against noisy data. Before testing our algorithm using experimental data, we conducted extensive simulations and the obtained results were in good agreement with the exact values, for up to 50% noise added to the "measured" data [15].

4. Conclusions

We have demonstrated the applicability of our T-matrix based algorithm for simultaneous recovery of shape parameters and concentration of cell suspensions embedded in scattering media using multispectral diffusing light measurements. Both spherical and non-spherical cells were examined. The recovered values of cellular morphology were validated by microscopy. For highly concentrated colloidal suspensions, the current particle scattering model needs some modifications to account for particle–particle interactions. This study is currently under way in our lab and the results will be reported in the near future.

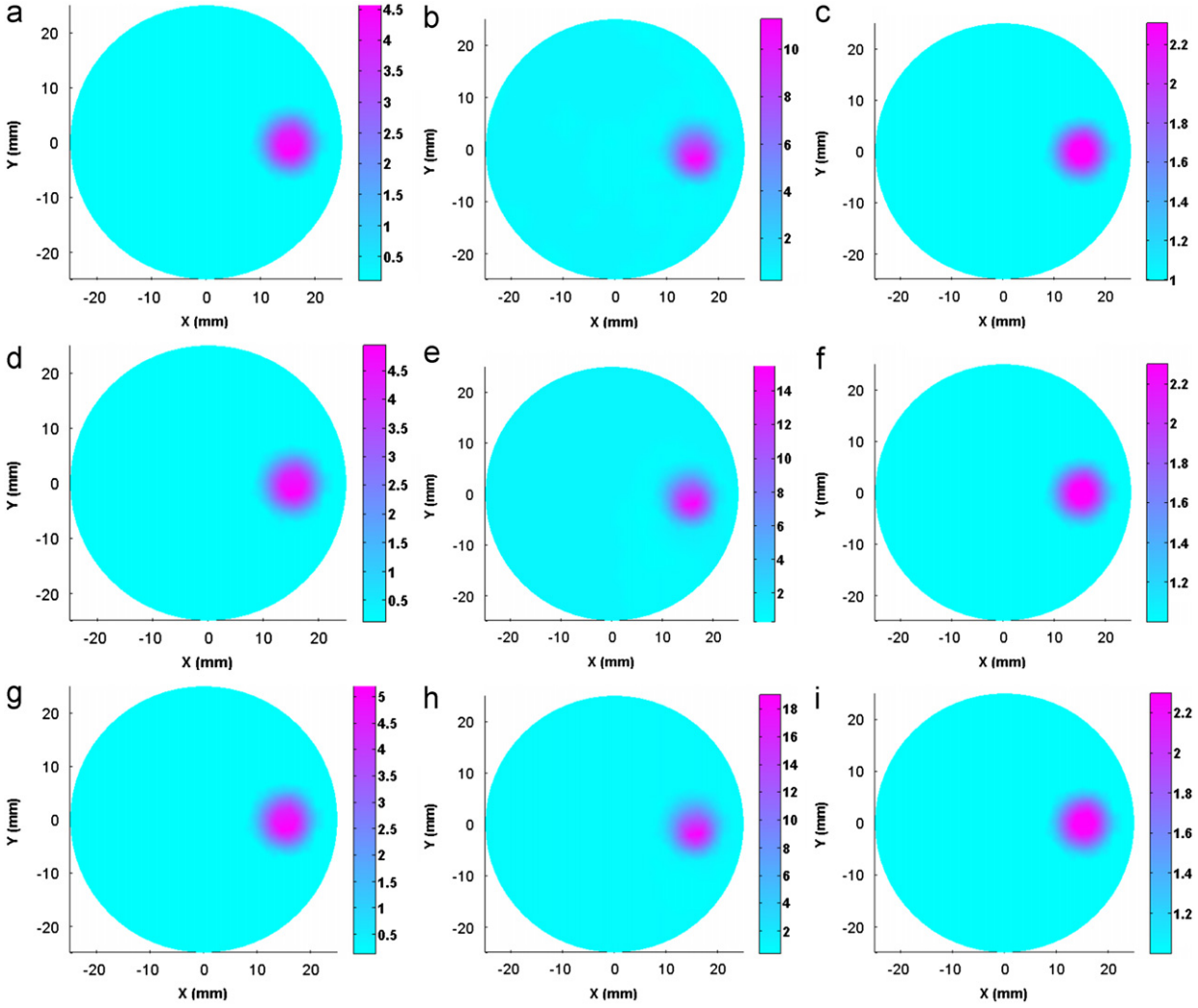

Fig. 5. Reconstructed particle size (a, d and g), concentration (b, e and h), and aspect ratio (c, f and i) of RBCs at three different concentrations (top row: 9%, middle row: 16%, and bottom row: 33%).

Acknowledgment

We would like to thank Prof. M. Mishchenko for providing the FORTRAN code used for preparing the T-matrix database. This research was supported in part by an NIH grant (R01 NS069848).

References

[1] C. Li, SR. Grobmyer, N. Massol, X. Liang, Q. Zhang, L. Chen, LL. Fajardo, H. Jiang, Medical Physics 35 (2008) 2493.
[2] M.G. Giacomelli, K.J. Chalut, J.H. Ostrander, A.H. Wax, IEEE Journal of Selected Topics in Quantum Electronics 16 (4) (2010) 900.
[3] V. Backman, R. Gurjar, K. Badizadegan, I. Itzkan, R.R Dasari, L.T Perelman, M.S. Feld, IEEE Journal of Selected Topics in Quantum Electronics 5 (4) (1999) 1019.
[4] George Matthew Bartlett, Lyndon Huang, Larcom, Huabei Jiang, Applied Optics 43 (2004) 1296.
[5] R.S. Gurjar, V. Backman, L.T. Perelman, I. Georgakoudi, K. Badizadegan, I. Itzkan, R.R. Dasari, M.S. Feld, Nature Medicine 7 (2001) 1245.
[6] A. Wax, V. Backman, Biomedical Applications of Light Scattering, McGraw-Hill, 2009.
[7] H. Jiang, Diffuse Optical Tomography: Principles and Applications, CRC Press, 2010.
[8] N. Riefler, T. Wriedt, Particle & Particle Systems Characterization 25 (3) (2008) 216.
[9] C. Tropea, Annual Review of Fluid Mechanics 43 (1) (2010) 399.
[10] M.I. Mishchenko, L.D. Travis, D.W. Mackowski, Journal of Quantitative Spectroscopy and Radiative Transfer 111 (11) (2010) 1700, 50 Years of JQSRT.
[11] M.I. Mishchenko, N.T. Zakharova, G. Videen, N.G. Khlebtsov, T. Wriedt, Journal of Quantitative Spectroscopy and Radiative Transfer 111 (4) (2010) 650.
[12] Donald D. Duncan, Michael E. Thomas, Applied Optics 46 (2007) 6185.
[13] I. Veselovskii, O. Dubovik, A. Kolgotin, T. Lapyonok, D. Summa, D.N. Whiteman, M. Mishchenko, D. Tanré, Journal of Geophysical Research 115 (D21203) (2010) 16.
[14] Michael G. Giacomelli, Kevin J. Chalut, Julie H. Ostrander, Adam Wax, Optics Letters 33 (2008) 2452.
[15] M.Reza Hajihashemi, Huabei Jiang, Applied Optics 50 (2011) 3896.
[16] M. Mishchenko, Journal of Quantitative Spectroscopy and Radiative Transfer 60 (3) (1998) 309.
[17] Florian Rene Michels, Foschum, Alwin Kienle, Optics Express 16 (2008) 5907.
[18] C. Li, H. Jiang, Optics Express 12 (25) (2004) 6313.
[19] Y. Han, XM. Liu, H. Liu, SC. Li, BC. Wu, LL. Ye, QW. Wang, ZL. Chen, Journal of Bioscience and Bioengineering 102 (5) (2006) 430.
[20] M. Takagi, T. Kitabayashi, S. Ito, M. Fujiwara, Journal of Biomedical Optics 12 (2007) 054010.
[21] Long Yi-Ren Chang, Hsu, Sien Chi, Applied Optics 45 (2006) 3885.
[22] M.S. Sinacore, D. Drapeau, S.R. Adamson, Molecular Biotechnology 15 (3) (2000) 249.
[23] A.M.K. Nilsson, Applied Optics 37 (1998) 2735.
[24] A. Karlsson, J. He, J. Swartling, S. Andersson-Engels, IEEE Transactions on Biomedical Engineering 52 (1) (2005) 13.
[25] Stephanos V. Tsinopoulos, Demosthenes Polyzos, Applied Optics 38 (1999) 5499.
[26] Gerhard Martina Meinke, Jürgen Müller, Helfmann, Moritz Friebel, Applied Optics 46 (2007) 1742.
[27] Z. Sun, C.D. Tomlin, E.M. Sevick-Muraca, Langmuir 17 (20) (2001) 6142.
[28] Z. Sun, E.M. Sevick-Muraca, Journal of Colloid and Interface Science 270 (2004) 329.